1-1-2015

A custom battery for operando neutron powder diffraction studies of electrode structure

Wei Kong Pang
University of Wollongong, wkpang@uow.edu.au

Vanessa Peterson
The Bragg Institute, Australian Nuclear Science And Technology Organisation, vep@ansto.gov.au

A custom battery for operando neutron powder diffraction studies of electrode structure

Abstract

Structure-property relations are central to understanding functional materials, and for battery research the use of neutron powder diffraction to reveal the atomistic and molecular-scale origin of battery performance characteristics is often essential. Although operando experiments of this kind are increasingly common as neutron sources and instrumentation advance, these experiments are hindered by the often large barrier presented by the preparation of whole batteries that yield a neutron diffraction signal from the electrode of interest that is sufficient to extract detailed structural information. This article presents a custom battery that is specifically designed for operando neutron powder diffraction. The battery is a pouch type and contains layers of positive and negative electrodes in a parallel-connecting stack. Importantly, the battery can be easily prepared in most laboratories, is configurable, and can be used with both lithium and sodium charge carriers. This paper provides some example operando neutron powder diffraction studies using this battery.

Keywords

neutron, studies, powder, electrode, operando, diffraction, structure, battery, custom

Disciplines

Engineering | Physical Sciences and Mathematics

Publication Details

Pang, W. Kong. & Peterson, V. K. (2015). A custom battery for operando neutron powder diffraction studies of electrode structure. Journal of Applied Crystallography, 48 280-290.

Journal of
Applied
Crystallography

ISSN 1600-5767

Received 18 September 2014
Accepted 13 January 2015

A custom battery for *operando* neutron powder diffraction studies of electrode structure

Wei Kong Pang[a,b] and Vanessa K. Peterson[a]*

[a]Australian Nuclear Science and Technology Organisation, Locked Bag 2001, Kirrawee DC, NSW 2232, Australia, and [b]Institute for Superconducting and Electronic Materials, University of Wollongong, NSW 2500, Australia. Correspondence e-mail: vanessa.peterson@ansto.gov.au

Structure–property relations are central to understanding functional materials, and for battery research the use of neutron powder diffraction to reveal the atomistic and molecular-scale origin of battery performance characteristics is often essential. Although *operando* experiments of this kind are increasingly common as neutron sources and instrumentation advance, these experiments are hindered by the often large barrier presented by the preparation of whole batteries that yield a neutron diffraction signal from the electrode of interest that is sufficient to extract detailed structural information. This article presents a custom battery that is specifically designed for *operando* neutron powder diffraction. The battery is a pouch type and contains layers of positive and negative electrodes in a parallel-connecting stack. Importantly, the battery can be easily prepared in most laboratories, is configurable, and can be used with both lithium and sodium charge carriers. This paper provides some example *operando* neutron powder diffraction studies using this battery.

1. Introduction

Increasing environmental and sustainability concerns have motivated the development of alternative and renewable-energy technologies, resulting in the intensive development of corresponding energy-storage devices, particularly for mobile use and where sources are intermittent. Lithium-ion batteries (LIBs) are at the forefront of portable battery technology and are widely used in electronic devices and integrated into electric vehicles (EVs) because of their higher energy density (both gravimetric and volumetric) and longer lifetime relative to other cell chemistries. Tesla Motors recently demonstrated a technological leap in LIB application in EVs, introducing EVs capable of achieving ~300 miles (~483 km) per charge, achieved through novel battery-pack assembly (Tesla Motors, 2014). Further LIB advancements though energy/power gains are restricted by the narrow operating window as a result of the limitations of both the LIB electrolyte and electrode electrochemistry (Tarascon & Armand, 2001; Goodenough & Kim, 2011). Moreover, the leading EV cathode chemistries, including $LiCoO_2$ and $Li(Ni_{1/3}Mn_{1/3}Co_{1/3})O_2$, contain toxic and expensive Co, with the world Co price currently set by LIB demand (Dillow, 2014). Hence, intensive research has been carried out to search for alternative and Co-free electrode materials that meet the needs of high-power applications. Additionally, the relatively low natural abundance of lithium presents a critical challenge to the sustainability of LIBs, leading to the emergence of sodium-ion batteries (SIBs), which have similar electrochemistry.

The electrochemical behaviour of materials is governed by the underlying structural and chemical evolutions, and a mechanistic understanding of the charge-carrier insertion/extraction process is critically important to advance new materials towards important LIB/SIB applications in emerging technologies. Neutron scattering plays a particularly important role in this research. The neutron scattering mechanism results in the sensitivity of neutron powder diffraction (NPD) to lighter elements such as lithium and oxygen in the presence of heavier atoms, enabling the direct measurement of lithium content and location within electrodes. Similarly, NPD may yield excellent signal contrast from near-neighbour elements on the periodic table such as the transition metals, of great benefit for the new generation of mixed transition metal electrodes.

Important to understanding electrode behaviour is the study of electrodes within whole batteries during charge and discharge. The relatively large penetration depth and nondestructive interaction with matter that neutrons offer couples with the fast detection ability of modern instrumentation to enable NPD to probe in real time the bulk crystallographic changes of electrodes in functioning batteries, with such studies known as *operando* studies. Ultimately, the possibility of using *operando* NPD to study not only the reaction mechanism and lattice parameter evolution of electrodes, but also the insertion/extraction mechanism of charge carriers and the determination of redox-active couples by tracking the transition metal valence *via* the oxygen to transition metal distance (Brown & Altermatt, 1985), is essential to the development of future battery technology. It is because of these benefits that *in situ* NPD is attracting increasing attention in the literature, with ~73% of the ~37 publications

using this method to investigate LIBs appearing since 2012 (Bergstöm *et al.*, 1998; Berg *et al.*, 2001; Rodriguez *et al.*, 2004, 2010; Rosciano *et al.*, 2008; Colin *et al.*, 2010; Sharma *et al.*, 2010, 2012; Du *et al.*, 2011; Sharma, Du *et al.*, 2011; Sharma, Reddy *et al.*, 2011; Dolotko *et al.*, 2012; Senyshyn *et al.*, 2012; Sharma & Peterson, 2012; Wang *et al.*, 2012; Bianchini *et al.*, 2013; Cai, An *et al.*, 2013; Godbole *et al.*, 2013; Hu *et al.*, 2013; Liu *et al.*, 2013; Roberts *et al.*, 2013; Senyshyn *et al.*, 2013; Sharma & Peterson, 2013*a*,*b*; Sharma *et al.*, 2013; Bobrikov *et al.*, 2014; Dolotko *et al.*, 2014; Pang, Peterson *et al.*, 2014*a*,*b*; Pang, Sharma *et al.*, 2014; Senyshyn *et al.*, 2014; Zinth *et al.*, 2014; Alam *et al.*, 2014; Vadlamani *et al.*, 2014; Pang, Alam *et al.*, 2014; Pang, Kalluri *et al.*, 2014; Brant *et al.*, 2014). Given the significant benefits of *in situ* and *operando* NPD to battery research, this relatively small number of publications reflects a combination of barriers to realizing such experiments, including limited access to neutron facilities, the difficulty of preparing neutron-friendly batteries and the often complex data analysis. Amongst these barriers, the preparation of a neutron-friendly battery yielding information from the electrode of interest sufficient for the extraction of detailed structural information is significantly high.

The interaction of neutrons with the many components within a battery needs to be considered during an NPD experiment. These components include the cathode, anode, positive and negative current collectors (aluminium and copper foil in most cases, with the copper being absent in a half-cell configuration), separator, electrolyte, and battery casing. In particular, the incoherent neutron scattering cross section of hydrogen (∼80.3 b) present in the traditionally organic electrolyte and separator, along with the battery casing, result in a high background and obscure the useful coherent neutron scattering from the electrodes. Deuterium has a significantly lower incoherent (∼2.0 *cf.* ∼80.3 b) and a significantly higher coherent neutron scattering cross section than hydrogen (∼5.6 *cf.* 1.8 b), meaning that deuterated electrolyte has a considerably reduced background and is often necessary to produce a measurable NPD signal from the electrodes in a battery. Similarly, the separator can be replaced with alternative hydrogen-free or -poor materials. Furthermore, an amount of the active electrode material sufficient to obtain a measurable signal is required, and the battery design must accommodate these relatively large amounts of electrode material. Finally, it is necessary to consider the structure of the component of interest when choosing battery components, to avoid (wherever possible) peak overlap. Table 1 summarizes the materials studied using *in situ* NPD and the types of batteries used. Aside from commercial batteries, previous *in situ* NPD studies have used coin-type, roll-over cylindrical and pouch-type custom-designed batteries.

The first *in situ* NPD battery experiment used a commercial cylindrical battery (18650-type), these offering the advantage of a relatively large electrode content (typically >15 g), relatively low electrolyte content and almost no sample preparation. The major drawback of using commercial batteries is the restricted range of available electrode chemistries, whereas it is necessary to use custom-designed batteries to research future electrode materials. Of the custom-designed battery types, half-cell-type batteries offer the lowest hydrogen content as only a single layer of separator and a relatively small amount of electrolyte are used in the design, and the casing is usually hydrogen free. In the first half-cell-type battery featuring a Pyrex tube, a significant amount of active material was used, but the relatively poor contact of the anode and cathode with the current collectors limited the electrochemical performance of the battery (Bergstöm *et al.*, 1998; Berg *et al.*, 2001). To improve this, constant mechanical pressure was applied to some half-cell-type batteries to ensure adequate contacts (Rosciano *et al.*, 2008; Colin *et al.*, 2010; Bianchini *et al.*, 2013; Godbole *et al.*, 2013; Vadlamani *et al.*, 2014). However, the main drawback of half-cell-type batteries for *operando* NPD is that they are technically difficult and expensive to construct. Further, the relatively small amount of active material in the half-cell-type battery also necessitates a longer NPD data collection time, reducing temporal resolution and restricting the derived kinetic information. The roll-over cylindrical battery design is a modification of the commercial 18650-type battery, using a tube casing (*i.e.* vanadium) that has a relatively small contribution to the collected NPD data. Whilst the roll-over battery has produced excellent results using *in situ* NPD, a significant drawback of the design is the technical degree of difficulty in its construction, with compactness of the roll-over difficult to achieve and failure leading to limited rate capability and capacity. Short circuits and disconnects are relatively easy to introduce to the roll-over design. These can be catastrophic to battery function and are detectable only once the expensive deuterated electrolyte has been added. Another drawback of the roll-over design is the presence of two layers of the hydrogen-containing material that separates the cathode and anode. Finally, the roll-over design is usually a half-cell configuration. The third type of custom-designed battery used for *in situ* NPD experiments is the pouch-type battery, featuring multiple parallel-connecting cells. The pouch-type battery is available commercially and thus has the same advantages as the 18650-type commercial battery. The disadvantages of the pouch-type battery for *in situ* NPD are also the same as for the 18650-type, in addition to a further complication arising from its non-annular geometry. Predominantly because of its ease of construction in a research-laboratory setting, the pouch-type battery is increasingly being used in NPD experiments. Liu *et al.* (2013) used a pouch-type battery containing a single stack of cathode/separator/anode/separator/cathode materials in an *in situ* NPD experiment. In this study, commercial polyvinylidene difluoride (PVDF, Immobilon-P, Millipore) separator and lithium hexafluorophosphate ($LiPF_6$) in ethylene and dimethyl carbonate as electrolyte were used. The single stack in this work restricted the amount of active material, despite the electrodes having a coated area density of approximately 8–12 mg cm^{-2}.

The pouch-type battery is increasingly being used in NPD experiments and is the focus of the present work in which we introduce a custom-designed pouch-type battery for *in situ* and *operando* NPD studies aimed at furthering electrode

Table 1
Summary of batteries used in *in situ* NPD studies of LIBs.

Year	Reference	Material studied	Cell configuration	Battery type
1998	Bergstöm *et al.* (1998)	$Li_xMn_2O_4$	Half	Pyrex tube-like half-cell
2001	Berg *et al.* (2001)	$LiMn_2O_4$	Half	Pyrex tube-like half-cell
2004	Rodriguez *et al.* (2004)	$LiCoO_2$ and graphite	Full	Commercial 18650-type
2008	Rosciano *et al.* (2008)	$LiNiO_2$	Half	Polyetheretherketone large coin-type half-cell
2010	Colin *et al.* (2010)	$Li_4Ti_5O_{12}$	Half	Polyetheretherketone large coin-type half-cell
2010	Rodriguez *et al.* (2010)	$LiFePO_4$ and graphite	Full	Commercial 18650-type
2010	Sharma *et al.* (2010)	$LiCoO_2$ and graphite	Full	Commercial 18650-type
2011	Du *et al.* (2011)	$Li_4Ti_5O_{12}$ and TiO_2	Half	Roll-over cylindrical V
2011	Sharma, Du *et al.* (2011)	MoS_2	Half	Roll-over cylindrical V
2011	Sharma, Reddy *et al.* (2011)	$Li(Co_{0.16}Mn_{1.84})O_4$	Half	Roll-over cylindrical V
2012	Dolotko *et al.* (2012)	$LiCoO_2$ and graphite	Full	Commercial 18650-type
2012	Senyshyn *et al.* (2012)	$LiCoO_2$ and graphite	Full	Commercial 18650-type
2012	Sharma *et al.* (2012)	$LiFePO_4$	Half	Roll-over cylindrical V
2012	Sharma & Peterson (2012)	$LiCoO_2$, $LiMn_2O_4$, $LiFePO_4$, graphite, $YFe(CN)_6$ and $FeFe(CN)_6$	Half	Roll-over cylindrical V
2012	Wang *et al.* (2012)	Graphite	Full	Commercial 18650-type
2013	Bianchini *et al.* (2013)	$LiFePO_4$ and $Li_{1.1}Mn_{1.9}O_4$	Half	Ti–Zn alloy large coin-type half-cell
2013	Cai, An *et al.* (2013)	$LiMn_2O_4$ and graphite	Full	Commerical pouch-type
2013	Godbole *et al.* (2013)	$Li_{1.1}(Ni_{1/3}Mn_{1/3}Co_{1/3})_{0.9}O_2$, $LiFePO_4$, $Li_4Ti_5O_{12}$ and graphite	Half	Al–Ti alloy large coin-type half-cell
2013	Hu *et al.* (2013)	V-doped $LiFePO_4$	Full	Commerical pouch-type
2013	Liu *et al.* (2013)	$xLi_2MnO_3{\cdot}(1-x)LiMO_2$ composite (x = 0, 0.5; M = Ni, Mn, Co)	Full	Single-stack pouch-type
2013	Roberts *et al.* (2013)	$LiFePO_4$	Half	Roll-over cylindrical Swagelock-type
2013	Senyshyn *et al.* (2013)	Graphite	Full	Commercial 18650-type
2013	Sharma & Peterson (2013*a*)	Graphite	Full	Commercial 18650-type
2013	Sharma & Peterson (2013*b*)	Graphite	Full	Commercial 18650-type
2013	Sharma *et al.* (2013)	$Li_{1+y}Mn_2O_4$	Full	Pouch-type
2014	Bobrikov *et al.* (2014)	$LiFePO_4$	Full	Commercial pouch-type
2014	Dolotko *et al.* (2014)	$Li(Ni_{1/3}Mn_{1/3}Co_{1/3})O_2$	Full	Commercial 18650-type
2014	Pang, Peterson *et al.* (2014*a*)	$Li_4Ti_5O_{12}$	Full	Pouch-type
2014	Pang, Sharma *et al.* (2014)	$LiNi_{0.5}Mn_{1.5}O_4$ and $Li_4Ti_5O_{12}$	Full	Pouch-type
2014	Senyshyn *et al.* (2014)	$LiCoO_2$ and graphite	Full	Commercial 18650-type
2014	Zinth *et al.* (2014)	Graphite	Full	Commercial 18650-type
2014	Alam *et al.* (2014)	$Li(Ni_{1/3}Mn_{1/3}Co_{1/3})O_2$ and Al-doped $Li(Ni_{1/2}Co_{1/2})O_2$	Full	Commercial 18650-type
2014	Pang, Peterson *et al.* (2014*b*)	$Li_4Ti_5O_{12}$	Full	Pouch-type
2014	Vadlamani *et al.* (2014)	$LiCoO_2$, $LiMn_2O_4$ and graphite	Full	Planar stacking-type with Si case
2014	Pang, Alam *et al.* (2014)	$Li(Ni_{1/3}Mn_{1/3}Co_{1/3})O_2$ and Al-doped $Li(Ni_{1/2}Co_{1/2})O_2$	Full	Commercial 18650-type
2014	Pang, Kalluri *et al.* (2014)	$Li(Ni_{1/3}Mn_{1/3}Fe_{1/3})O_2$	Full	Pouch-type
2014	Brant *et al.* (2014)	$Li_{0.18}Sr_{0.66}Ti_{0.5}Nb_{0.5}O_3$	Half	Roll-over cylindrical V

research. The design is a modification of the commercial pouch-type battery and is relatively easy to prepare in a standard laboratory. The battery contains only one layer of hydrogen-poor separator to avoid short circuiting, is filled with deuterated electrolyte and is able to accommodate a relatively large amount of active material, enabling high temporal resolution. The battery can be scaled according to the availability of electrode materials, with the practical upper limit determined by the size of the neutron beam and the time required for charge/discharge of the battery. In the following sections we present the design of the pouch-type battery and discuss through examples aspects of its use in examining electrode structure.

2. Experimental

2.1. The neutron-friendly battery construction

The pouch-type battery specially designed for and used in the collection of *in situ* NPD data is shown in Fig. 1. The cathodes and anodes are conventionally prepared. Typically, the active electrode material is mixed with PVDF binder and acetylene black (carbon black) in the weight ratio of 83:7:10 in an adequate amount of *N*-methyl-2-pyrrolidinone to form a slurry. The slurry is tape-cast onto the current collector, aluminium (for the cathode) or copper (for the anode) foil, and dried at 393 K for 24 h. A coating thick enough to achieve an areal density of ∼4–6 mg cm^{-2} is used. The electrodes are cut into 1.5 × 6 cm strips with a 1.5 × 4 cm coated area, as shown in Fig. 2. Immobilon-P PVDF membrane (Millipore) is used as a separator for a LIB and glass-fibre membrane is used for a SIB. PVDF contains ∼3.15 wt% hydrogen and glass-fibre is hydrogen free, whereas conventional polypropylene separator consists of ∼14.4 wt% hydrogen. The battery is prepared by stacking anode/separator/cathode layers in parallel, as shown in Fig. 1(*a*). The stack is tightened with Kapton tape (Fig. 1*b*) and placed in an Ar-filled glove box to dry for at least 24 h. The stack is then wrapped in a polypropylene-coated aluminium pouch (Fig. 1*c*) and heat sealed, with one side open for electrolyte injection. The typical thickness of a battery is ∼0.6–0.8 cm including the separator, the electrodes and the aluminium pouch casing. The pouch

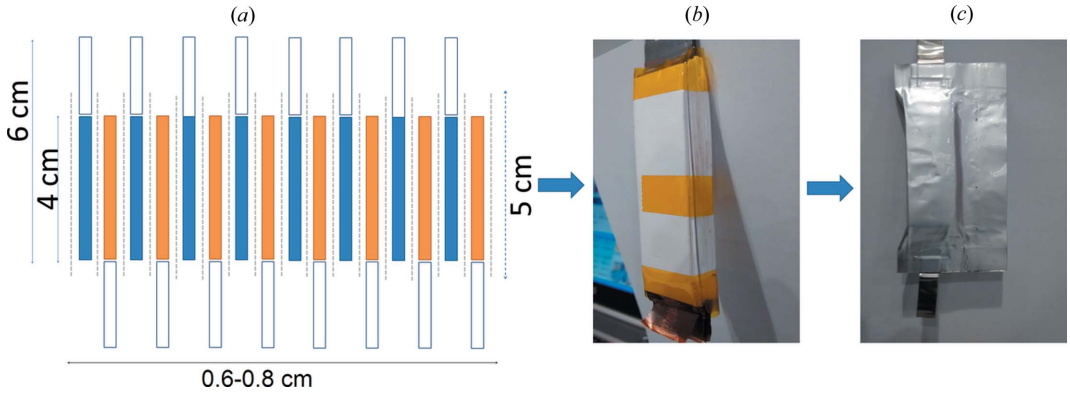

Figure 1
Pouch-type battery for use in *operando* NPD. (*a*) Schematic of parallel-connected cathode/separator/anode layers, where cathode layers are blue and anode layers are orange, and the connecting arms are shown in white. (*b*) Electrode and separator assembly. (*c*) Final battery sealed in the Al pouch. Fig. 1c adapted from Pang, Peterson *et al.* (2014*b*).

casing is ∼0.16 mm-thick aluminium foil, with the outer surface coated with thin polyamide and the inner surface coated with thin polyester. The polyamide/aluminium/polyester contains hydrogen, and the contribution of these components to the NPD data is not ignorable (see Fig. S1[1]).

The inner polyester layer is used for heat sealing and protecting the electrode stack from short circuits. The outer polyamide layer can be removed by light sanding, reducing the hydrogen content further. As shown in Fig. 1(*c*), the pouch seals are along all sides with the exception of one long axis, which is formed from the original fold. Prior to the neutron experiment, deuterated electrolyte solution is injected before the remaining edge is heat sealed. For a LIB, the electrolyte solution is typically 1 *M* $LiPF_6$ in a 1:1 volume ratio of deuterated dimethyl carbonate to deuterated ethylene carbonate. For a SIB, the electrolyte solution is typically 1 *M* $NaClO_4$ in deuterated propylene carbonate (d-PC). After injecting the electrolyte and sealing the pouch, the battery is stored in an Ar-filled glove box for at least 24 h, during which time the battery wets, after which it is ready for use.

2.2. Comparison of separators

NPD data of polypropylene (Celgard@2300, Celgard), PVDF (Immobilon-P, Millipore) and glass fibre (APFF14250, Millipore) separators were collected and their patterns compared and discussed with respect to use in the pouch-type battery. Data were collected on WOMBAT (Studer *et al.*, 2006), the high-intensity neutron powder diffractometer at the Open-Pool Australian Lightwater (OPAL) research reactor at the Australian Nuclear Science and Technology Organisation (ANSTO). WOMBAT features an area detector that continuously covers 120° in 2θ and a relatively intense neutron beam, allowing for the rapid collection of data. Data were collected at 2.4198 (1) Å, determined using the LaB_6 NIST standard reference material 660b, for 3 min.

[1] Supporting information for this paper is available from the IUCr electronic archives (Reference: KS5451).

2.3. Neutron diffraction

Prior to an *in situ* NPD battery experiment, X-ray powder diffraction (XRPD) data and high-resolution NPD data are generally used to characterize the as-prepared active materials. For the examples presented here, high-resolution NPD data were collected using ECHIDNA, the high-resolution neutron powder diffractometer at the OPAL research reactor at the ANSTO (Liss *et al.*, 2006). The *in situ* NPD data presented in this work were collected using WOMBAT. This instrument has been previously successfully used for *operando* NPD experiments on battery materials (Sharma *et al.*, 2010, 2012, 2013; Du *et al.*, 2011; Sharma, Du *et al.*, 2011; Sharma, Reddy *et al.*, 2011; Sharma & Peterson, 2012, 2013*a*,*b*; Hu *et al.*, 2013; Pang, Peterson *et al.*, 2014*a*,*b*; Pang, Sharma *et al.*, 2014; Pang, Alam *et al.*, 2014; Alam *et al.*, 2014; Pang, Kalluri *et al.*, 2014; Brant *et al.*, 2014). The experimental setup during the NPD experiments in which data are obtained during the battery cycling is shown in Fig. 3. The pouch-type battery is

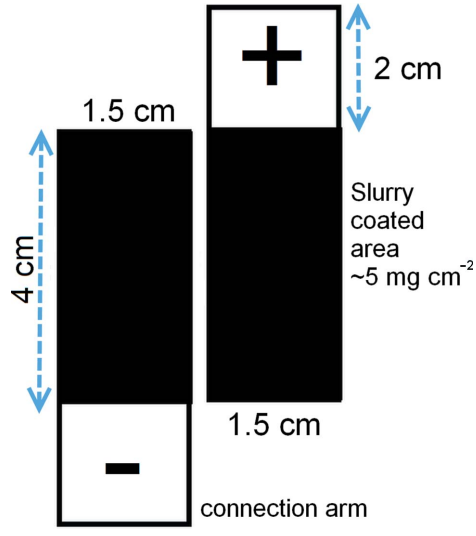

Figure 2
Schematic of the prepared electrodes for the custom *operando* NPD pouch-type cell.

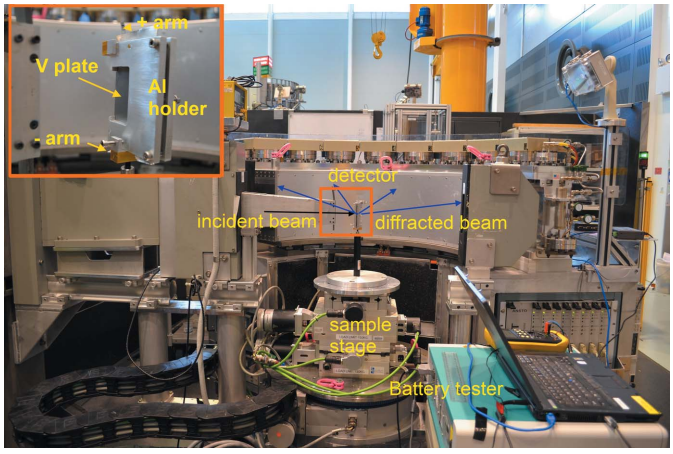

Figure 3
Experimental setup used for *operando* battery research with WOMBAT.

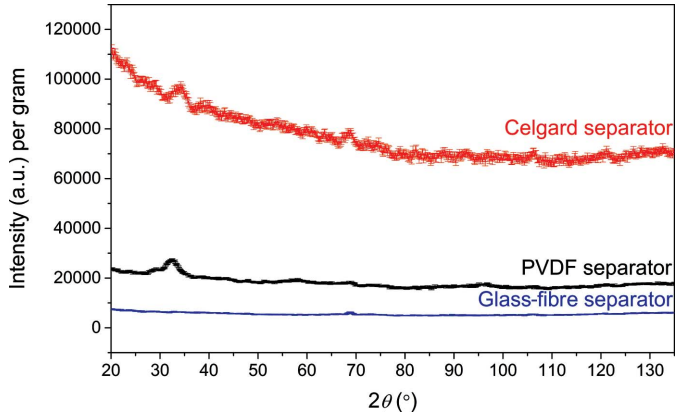

Figure 4
NPD patterns of polypropylene (Celgard), polyvinylidene difluoride (PVDF) and glass-fibre separators.

mounted in a purpose-built aluminium frame that holds a vanadium plate that compresses the battery and ensures contact between the electrodes and separator layers (shown in the inset of Fig. 3). The frame is compatible with WOMBAT's sample stage and easily mounted so that sample translation and rotation can be performed for battery alignment. The battery is held in the frame with the unsealed edge of the pouch (formed from the original aluminium-sheet fold) oriented 90° to the incident neutron beam and closest to the detector. A neutron beam of 1 (width) × 3 cm (height) is used, illuminating the half of the battery that is ∼0.8 cm from the outer edge exposed to the neutron beam. The battery volume probed by the neutrons in this configuration is 0.8 (width) × 0.8 (thickness) × 4.0 cm (height). The similar width and thickness of the sampled volume provides a relatively equal incident and scattered neutron path length, simulating an annular sample. In this way, the background of the NPD pattern remains flat even in the case of significant neutron absorption, simplifying analysis and enabling higher-accuracy intensity extraction. This experimental method has enabled the *in situ* NPD data to be analysed using both Rietveld and single-peak fitting methods, providing a detailed, atomic level mechanistic understanding of the battery's performance characteristics and the structure–function relation of the active materials.

3. Results and discussion

3.1. Separator selection

The cathode and anode are kept apart using a separator to avoid short circuits. The separator is usually an organic compound that contains hydrogen and is detrimental to the NPD data, such as the commercial Celgard material. Depending on the cell construction, the amount of Celgard may be sufficiently small to enable NPD measurement of the active material, particularly when the quantity of active material is relatively large such as in the commercial 18650-type (Sharma *et al.*, 2010; Hu *et al.*, 2013; Sharma & Peterson, 2013*a*) and some pouch-type (Cai, An *et al.*, 2013; Hu *et al.*, 2013) batteries. Replacement of the Celgard separator with PVDF or glass-fibre separators reduces or eliminates, respectively, the amount of hydrogen in the separator.

The chemical stability, porosity, pore size and wettability of the separator are critical for battery function (Zhang, 2007; Venugopal *et al.*, 1999). Whilst the chemical stability and wettability of the PVDF and glass-fibre separators are suitable for their use with the organic electrolytes used in LIB and SIB batteries, the pore size of the separator must be smaller than the particle size of the electrode materials for effective separation. We note that pore topology can influence this significantly. Although PVDF has a relatively large pore size (∼0.45 µm) compared to Celgard (∼0.064 µm), this material has been used successfully as a separator in batteries studied with *operando* NPD (Pang, Peterson *et al.*, 2014*a*; Pang, Sharma *et al.*, 2014). Glass fibre has a pore size even larger than PVDF, of ∼0.7 µm, combined with a high porosity (∼90%). This separator has been shown to be suitable for use with SIBs (Yabuuchi *et al.*, 2012) but not with LIBs, the latter requiring porosity no greater than ∼40% as a result of the different electrolytes used (Zhang, 2007; Venugopal *et al.*, 1999). NPD data of Celgard, PVDF and glass-fibre separators, with intensity shown per gram of material, are shown in Fig. 4. Celgard is polypropylene, $(C_3H_6)_n$, and contains significantly more hydrogen than PVDF, $(C_2H_2F_2)_n$, resulting in a higher background in the NPD pattern. Although glass fibre is hydrogen free, it contains boron (originating from B_2O_3), with a significantly high neutron absorption cross section, resulting in a reduced signal owing to attenuation. The relatively small amount of boron in the glass fibre (∼3.32 wt%) means that the resultant beam attenuation does not interfere significantly with the NPD measurement. Taken together, these results point to PVDF and glass-fibre separators as the most suitable for use in pouch-type LIBs and SIBs, respectively, for *operando* NPD experiments.

3.2. *Operando* NPD experiments with the customized pouch-type battery

We present several example studies that provided insight into the structural and chemical evolutions of electrodes that

govern the electrochemical function of batteries using real-time non-equilibrium NPD with the pouch-type battery. These studies have allowed the extraction of information ranging from the electrode phase and structural evolution, to details concerning the charge-carrier location and quantity in the electrode during charge/discharge.

3.2.1. The $Na_{2/3}(Fe_{1/2}Mn_{1/2})O_2$ cathode for use in a SIB. P2-type $Na_{2/3}(Fe_{1/2}Mn_{1/2})O_2$ (NFMO) has been explored for use as a cathode in SIBs. NFMO has $P6_3/mmc$ symmetry.

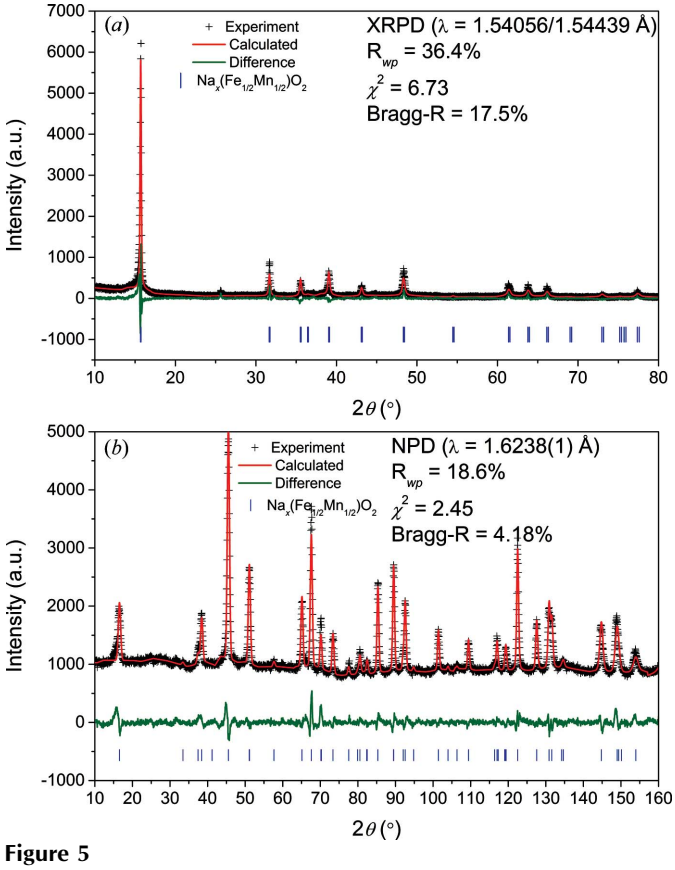

Figure 5
(*a*) XRPD and (*b*) NPD Rietveld refinement profiles and data of $P6_3/mmc$ $Na_{2/3}(Fe_{1/2}Mn_{1/2})O_2$. Vertical bars are reflection positions.

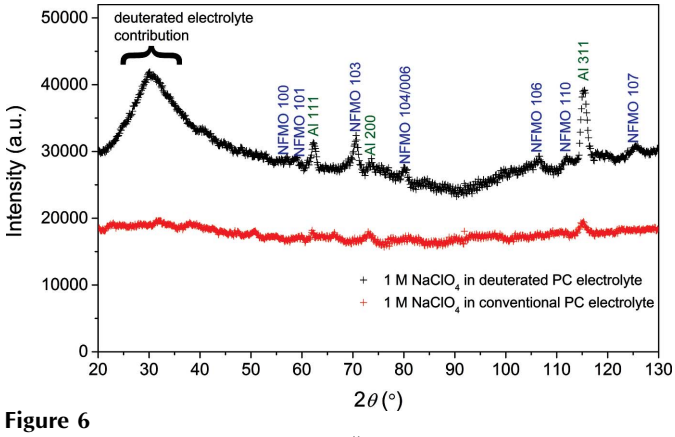

Figure 6
NPD patterns of $Na_{2/3}(Fe_{1/2}Mn_{1/2})O_2$||hard-carbon pouch-type batteries filled with deuterated PC electrolyte (black) and conventional hydrogen-containing PC electrolyte (red).

XRPD and NPD patterns of NFMO and their corresponding Rietveld refinement profiles are shown in Figs. 5(*a*) and 5(*b*), respectively. In this P2-type layered metal oxide, Na ions are accommodated at two locations between the ordered FeO_2 and MnO_2 hybrid layers, where Fe and Mn share the 2*a* site. The X-ray scattering power of Na and O are significantly lower than for Fe and Mn. Consequently, the XRPD intensity of the NFMO 002 reflection (at 15.68° in 2θ), where the NFMO (002) plane contains transition metals as shown in Fig. S2(*a*), is overwhelmingly stronger than the other reflections. By comparison, neutrons offer excellent contrast in the

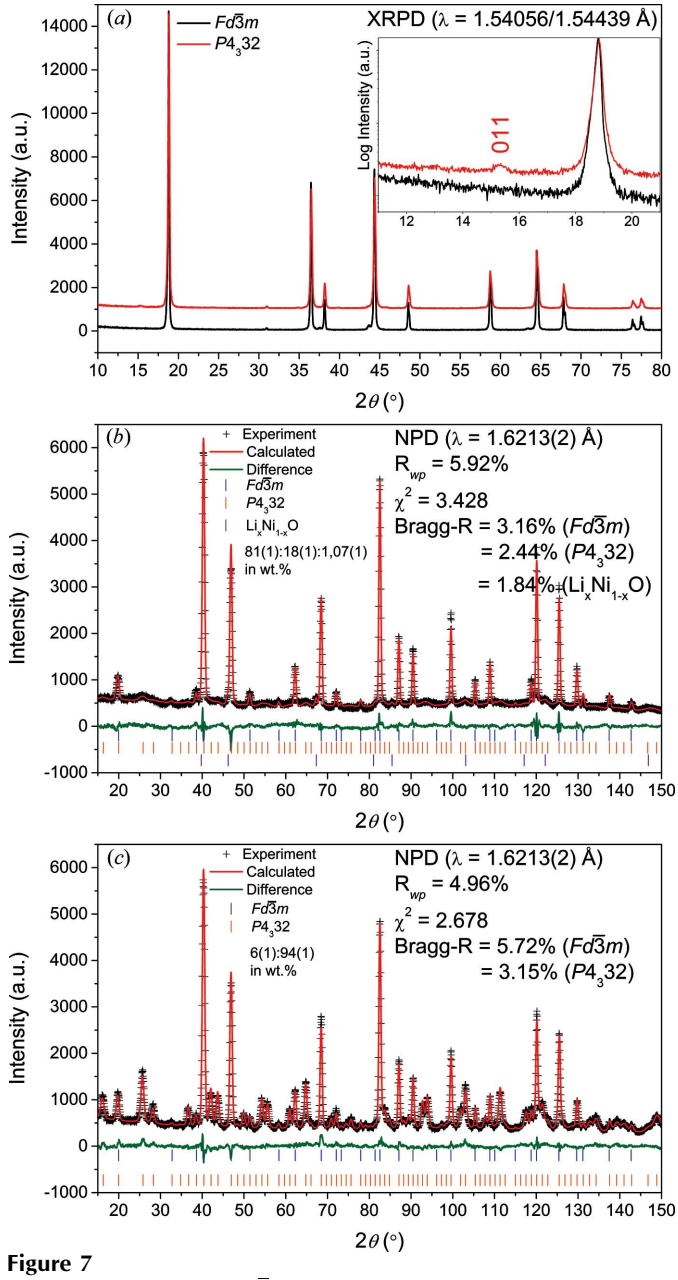

Figure 7
(*a*) XRPD patterns of $Fd\bar{3}m$ (black) and $P4_332$ (red) $LiNi_{0.5}Mn_{1.5}O_4$ phases. Rietveld refinement profiles of (*b*) $Fd\bar{3}m$ and (*c*) $P4_332$ $LiNi_{0.5}Mn_{1.5}O_4$ phases. Figures of merit include the weighted profile factor (R_{wp}), the Bragg statistical reliability factor (Bragg-R), and the goodness of fit (χ^2). Vertical bars are reflection positions for each phase.

coherent neutron scattering lengths between these elements, these being ~3.4 fm for Na, ~5.8 fm for O, ~9.5 fm for Fe and ~−3.7 fm for Mn, meaning that the NPD pattern for this material looks significantly different from that obtained using X-rays and, importantly, that the information is not dominated by the scattering from the transition metals. The additional information present in the NPD data makes the structure refinement more likely to yield a correct and unique solution than that achieved using XRPD.

NFMO can be combined with a non-graphitizable (hard carbon) anode in a SIB (Ponrouch *et al.*, 2013). A high-resolution NPD pattern of hard carbon is shown in Fig. S3. Two pouch-type batteries were assembled with an NFMO cathode, a hard-carbon anode and glass-fibre separator. One was filled with 1 *M* $NaClO_4$ in d-PC and the other with 1 *M* $NaClO_4$ in conventional hydrogen-containing PC. The NPD patterns of the NFMO||hard-carbon pouch-type batteries are shown in Fig. 6. The NPD pattern from the battery filled with conventional electrolyte features a background from the hydrogen that completely obscures the coherent neutron scattering from the cathode, with only the strongest reflection from the Al casing barely visible. In the NPD data for the battery containing the d-PC, Bragg reflections are visible from the cathode, Al casing and current collectors, with broadened peaks from the hard carbon (as shown in Fig. S3) not clearly distinguishable. A broad feature at ~30° in 2θ is also observed and attributed to the liquid structure factor of the d-PC, visible as a result of the significant coherent neutron scattering length of deuterium (~6.7 fm). Deuterated electrolytes are therefore clearly required for successful *operando* NPD experiments using this pouch-type battery.

3.2.2. Phase evolution of the disordered $LiNi_{0.5}Mn_{1.5}O_4$ cathode. Spinel $LiNi_{0.5}Mn_{1.5}O_4$ is considered a promising cathode material for use in LIBs owing to its high energy density as a result of a 4.7 V (*versus* Li/Li^+) plateau, in addition to its excellent cycling performance and high rate capability that are provided by its stable three-dimensional structure within the 3.0–5.0 V window (Ohzuku *et al.*, 1999; Ariyoshi *et al.*, 2004). $LiNi_{0.5}Mn_{1.5}O_4$ crystallizes into either the ordered primitive $P4_332$ phase, with distinct cationic arrangements of Li^+ (8*c*), Ni^{2+} (12*d*) and Mn^{4+} (4*b*), or the disordered face-centred $Fd\bar{3}m$, phase where 16*d* sites are shared by Ni^{2+} and Mn^{4+} and 8*a* sites are occupied by Li, as shown in Figs. S2(*a*) and 2(*b*) (Pasero *et al.*, 2008; Le *et al.*, 2011; Shiu *et al.*, 2013). As a result of the relatively poor contrast of the Mn and Ni X-ray scattering lengths, XRPD cannot easily distinguish these two phases, as shown in Fig. 7(*a*). The XRPD patterns of the structures shown in Fig. 7(*a*) differ only by the weak $P4_332$ 011 reflection (appearing at 15.32° in 2θ), which is

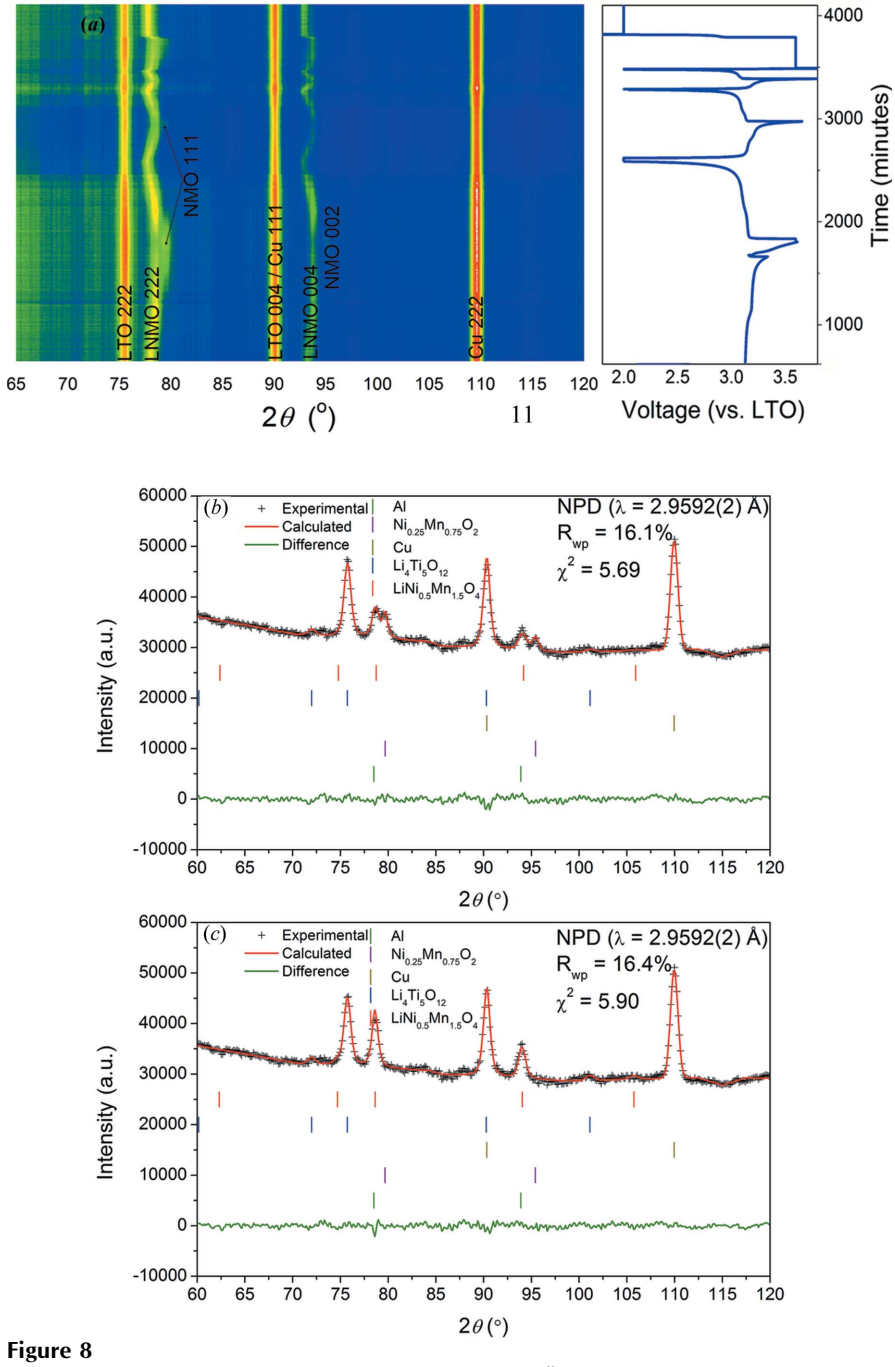

Figure 8
Contour plot of *operando* NPD data of an $LiNi_{0.5}Mn_{1.5}O_4$||$Li_4Ti_5O_{12}$ pouch-type battery during charge and discharge (*a*) and associated Rietveld refinement profiles collected in the (*b*) discharged and (*c*) charged state. LTO = $Li_4Ti_5O_{12}$, LNMO = $LiNi_{0.5}Mn_{1.5}O_4$ and NMO = $Ni_{0.25}Mn_{0.75}O_2$.

barely visible on a logarithmic scale. The similarity of the lattice parameters of these two phases means that NPD is required to definitively distinguish $Fd\bar{3}m$ and $P4_332$ $LiNi_{0.5}Mn_{1.5}O_4$ (Pang, Sharma *et al.*, 2014; Cai, Liu *et al.*, 2013; Bhaskar *et al.*, 2010; Shiu *et al.*, 2013), enabled by the very different coherent neutron scattering lengths of Mn (∼−3.7 fm) and Ni (∼10.3 fm). High-resolution NPD patterns and Rietveld refinement profiles for $Fd\bar{3}m$ and $P4_332$ $LiNi_{0.5}Mn_{1.5}O_4$ are shown in Figs. 7(*b*) and 7(*c*), which were used to characterize the cathode material in the corresponding pouch-type LIB studied using *operando* NPD (Pang, Sharma *et al.*, 2014). Ordered $P4_332$ $LiNi_{0.5}Mn_{1.5}O_4$ exhibits a relatively poorer rate capability and cycling performance compared to the disordered $Fd\bar{3}m$ material. The ordered spinel undergoes two cubic to cubic two-phase reactions, between $LiNi_{0.5}Mn_{1.5}O_4$ with a = 8.17 Å and $Li_{0.5}Ni_{0.5}Mn_{1.5}O_4$ with a = 8.09 Å at the $Ni^{2+/3+}$ transition, and between $Li_{0.5}Ni_{0.5}Mn_{1.5}O_4$ with a = 8.09 Å and $Ni_{0.5}Mn_{1.5}O_4$ with a = 8.00 Å at the $Ni^{3+/4+}$ transition. These include transformation during electrochemical cycling to an intermediate phase exhibiting $Fd\bar{3}m$ symmetry, suggesting a lower structural reversibility of the $P4_332$ form than that of the $Fd\bar{3}m$ form, especially at high rates (Kim, Myung *et al.*, 2004; Kim, Yoon *et al.*, 2004; Ariyoshi *et al.*, 2004).

The phase evolution of the disordered $LiNi_{0.5}Mn_{1.5}O_4$ phase was studied using *operando* NPD with the customized $LiNi_{0.5}Mn_{1.5}O_4||Li_4Ti_5O_{12}$ pouch-type battery (Pang, Sharma *et al.*, 2014). This work reported the mechanistic detail of the phase evolution of the $Fd\bar{3}m$ $LiNi_{0.5}Mn_{1.5}O_4$ for the first time. A contour plot of the *operando* NPD data of the battery during charge and discharge is shown in Fig. 8(*a*), with Figs. 8(*b*) and 8(*c*) showing the Rietveld refinement profiles using the NPD data collected in the discharged and charged battery states, respectively. The battery contains ∼600 mg of active cathode material and the loading ratio between the anode and cathode was designed to be 1.1 to 1 in capacity (mAh). At the chosen neutron wavelength (∼2.41 Å) on WOMBAT, a collection time of 5 min gave a signal of sufficient quality for constrained Rietveld analysis, with the quality of the information governed by accessible Q range as well as peak intensity, definition and resolution. The battery delivered 63.1, 47.0 and 27.9 mAh at applied currents of 5, 9 and 18 mA, respectively, and reasonable coulombic efficiency up to 93%. Both good signal quality and good battery performance, as achieved here, are necessary for such successful *operando* NPD experiments. The Rietveld analysis results were supplemented using peak-fitting analysis, and this approach enabled both the phase composition of the cathode and the oxygen positional parameter to be obtained during battery charge/discharge, with the latter used as an indicator of the transition metal valence. This work revealed a two-phase reaction producing the $Ni_{0.25}Mn_{0.75}O_2$ secondary phase with lattice parameter 4.000 (7) Å. Further, the lithium content at the 8*a* site was obtained, and alongside the position of the oxygen atom (32*e* site), these are correlated to the battery state of charge and delithiation/lithiation processes. Overall, the *operando* NPD study using the pouch-type LIB (Pang, Sharma *et al.*, 2014) revealed that the disordered $Fd\bar{3}m$ $LiNi_{0.5}Mn_{1.5}O_4$ cathode undergoes solid-solution and two-phase reactions that are associated with the Ni^{2+}/Ni^{3+} and Ni^{3+}/Ni^{4+} redox couples, respectively.

3.2.3. Phase evolution of zero-strain $Li_4Ti_5O_{12}$ anodes. Spinel $Li_4Ti_5O_{12}$ is a well known zero-strain insertion compound that is being used as an alternative anode to the widely used carbonaceous materials. $Li_4Ti_5O_{12}$ exhibits an exceptionally high rate performance, excellent cycling stability

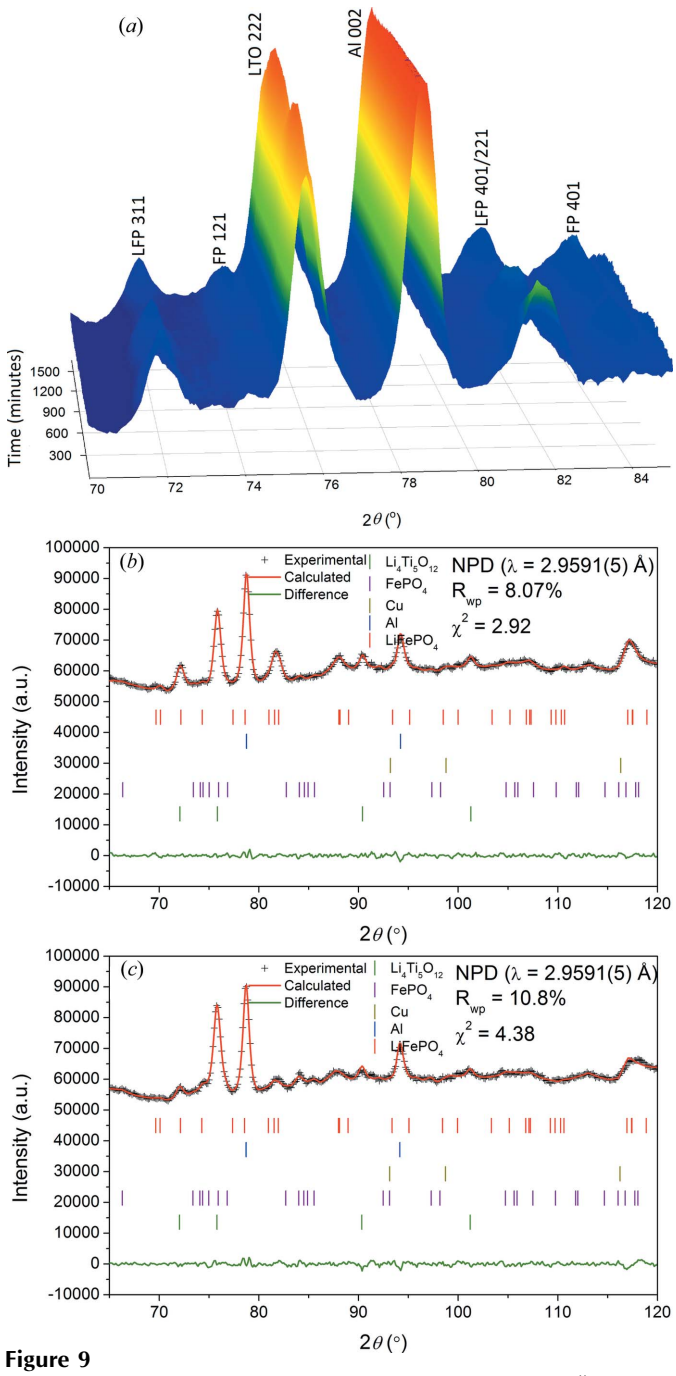

Figure 9
(*a*) Contour plot of *operando* NPD data from the $LiFePO_4||Li_4Ti_5O_{12}$ pouch-type battery during charge/discharge. Rietveld refinement profiles using NPD data collected in the (*b*) discharged and (*c*) charged battery state are also shown. LFP = $LiFePO_4$, FP = $FePO_4$ and LTO = $Li_4Ti_5O_{12}$.

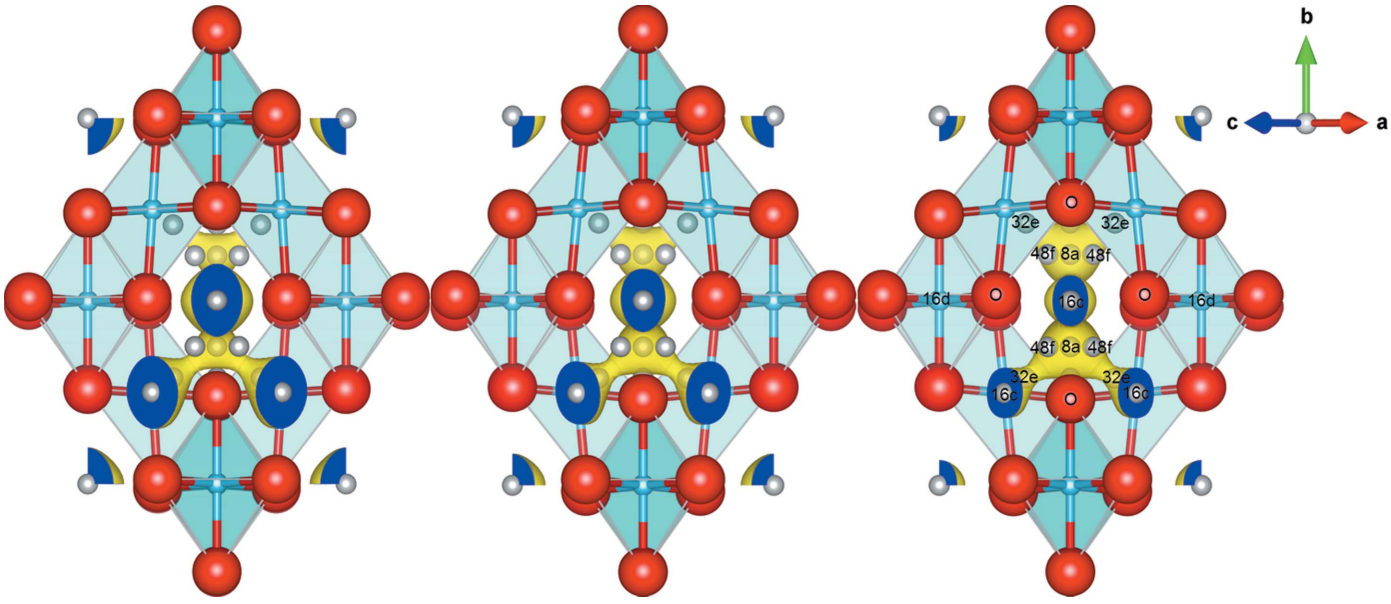

Figure 10
Fourier difference maps depicting the negative nuclear-density (yellow) overlaid with the refined $Li_{4+z}Ti_5O_{12}$ structure in the battery's charged (left), half-charged (middle) and discharged states (right). O atoms are shown in red, Li is shown in grey with sites marked, and Ti and Li at the 16*d* site are shown in cyan (and marked). Contour levels (yellow) are shown at the same scale for the three maps. The residual negative nuclear density that surrounds the 32*e* site, between the 8*a* and 16*c* sites, indicates the possibility that the site is involved in Li diffusion, which would lower the energy barrier to diffusion as suggested by Laumann *et al.* (2011). Figure adapted from Pang, Peterson *et al.* (2014*a*).

and good Li-insertion electrochemistry with a formal potential of ∼1.55 V *versus* Li^+/Li as an anode in LIBs (Ohzuku *et al.*, 1995; Scharner *et al.*, 1999; Panero *et al.*, 2001; Cho *et al.*, 2001; Ronci *et al.*, 2002).

The structural evolution of $Li_4Ti_5O_{12}$ was successfully studied using *operando* NPD with the pouch-type battery containing approximately 680 mg of active anode. The ∼4:6 mass ratio of the anode:cathode in the battery was chosen so that the anode was the limiting electrode, forcing the anode's full lithiation/delithiation and enabling the Li^+ insertion/extraction mechanisms to be characterized. The battery delivered a discharge capacity of 49.1 mAh, at a constant current of 11 mA when cycling in the 1.0–3.0 V window (*versus* $Li_4Ti_5O_{12}$) with a smooth charge/discharge curve, indicating good functionality. The quality of the NPD signal from electrodes in the pouch-type battery was sufficient to allow Rietveld refinement. Fig. 9 shows the *operando* NPD data and typical Rietveld refinement profiles of the battery. Lithiation/delithiation of the $Li_4Ti_5O_{12}$ was observed to occur alongside the typical two-phase transition of $LiFePO_4$ during the galvanostatical charging and discharging. The transition of the anode was modelled as a solid-solution reaction to reveal the underlying mechanism for the particle-size-induced changes in battery performance (Pang, Peterson *et al.*, 2014*a*). The anode phase composition, the lattice parameter, the oxygen positional parameter, and the occupancy of the 8*a* and 16*c* sites by lithium could be extracted as a function of battery charge and discharge using these data.

The measured lattice parameter changes are reconciled with the occupancy variation of Li at specific sites within the $Li_4Ti_5O_{12}$ crystal structure, and this work found that Li migrates from the 8*a* to 16*c* sites in the spinel structure. The determination of Li-diffusion paths in electrodes is extremely difficult using NPD data from whole batteries. To understand the Li-diffusion pathway in the anodes, we examined the nuclear-density maps produced using Fourier difference methods and the refined anode phases with Li removed (but after refinement). This was done for NPD data measured in the charged, half-charged and discharged states that were summed over two data sets. The analysis of these Fourier difference nuclear-density maps indicated that, in addition to the 8*a* and 16*c* sites, the 32*e* site is also involved in the diffusion of Li in the zero-strain anode (Fig. 10). Rietveld refinement results are again supported by the changes in peak position and intensity determined using peak fitting (Pang, Peterson *et al.*, 2014*a*). In the reported work, we also present a comparison of the Li^+ insertion/extraction mechanisms of $Li_4Ti_5O_{12}$ with different particle sizes, giving insight into how battery performance may be improved. The results all point to an increase in the number of Li ions migrating as a result of reduced path length in the smaller-particle-sized anode rather than a change in Li-migration pathway. Despite the similar trends of $Li_4Ti_5O_{12}$ lattice evolution and Li location during battery cycling, the smaller-particle-sized anode undergoes a much faster rate of change, 20.7 (3)% during lithiation and 5.5 (14)% during delithiation, than its larger-particle-sized counterpart, consistent with the larger measured capacity.

4. Conclusion

Neutron powder diffraction is exceptionally useful and in many cases required to determine the true crystallography of electrode materials for use in lithium- and sodium-ion batteries. *In situ* neutron powder diffraction experiments are

becoming increasingly popular, with *operando* experiments capable of revealing the structure evolution of the electrode materials during battery operation. This information underpins battery performance and is critical to progressing new battery materials for application in emerging technologies. A main challenge in such experiments is the preparation of 'neutron-friendly' batteries that enable a good neutron scattering signal from the electrodes of interest to be gained without compromising battery function. In this work, we present a pouch-type battery with multiple parallel-connecting cells, specifically designed for *operando* neutron powder diffraction studies of electrode materials. The battery is composed of polyvinylidene difluoride or glass-fibre separators, for use with lithium- and sodium-ion batteries, respectively, and contains deuterated electrolyte. The battery can be easily prepared in most laboratories. We have outlined the battery design and use, and detailed the type of information that can be obtained with the battery and the data analysis approaches taken to obtain this information.

The authors would like to thank their collaborators involved in battery research using the pouch-type battery in *operando* neutron powder diffraction experiments, notably Dr Neeraj Sharma from the University of New South Wales. The authors are also grateful to the Bragg Institute technical staff, particularly Dr Norman Booth and Mr Mark New, for their support and assistance.

References

Alam, M., Hanley, T., Pang, W. K., Peterson, V. K. & Sharma, N. (2014). *Powder Diffr.* **29**, S35–S39.
Ariyoshi, K., Iwakoshi, Y., Nakayama, N. & Ohzuku, T. (2004). *J. Electrochem. Soc.* **151**, A296–303.
Berg, H., Rundlöv, H. & Thomas, J. O. (2001). *Solid State Ionics*, **144**, 65–69.
Bergstöm, Ö., Andersson, A. M., Edström, K. & Gustafsson, T. (1998). *J. Appl. Cryst.* **31**, 823–825.
Bhaskar, A., Bramnik, N. N., Senyshyn, A., Fuess, H. & Ehrenberg, H. (2010). *J. Electrochem. Soc.* **157**, A689–A695.
Bianchini, M., Leriche, J. B., Laborier, J.-L., Gendrin, L., Suard, E., Croguennec, L. & Masquelier, C. (2013). *J. Electrochem. Soc.* **160**, A2176–A2183.
Bobrikov, I. A., Balagurov, A. M., Hu, C.-W., Lee, C.-H., Chen, T.-Y., Deleg, S. & Balagurov, D. A. (2014). *J. Power Sources*, **258**, 356–364.
Brant, W. R., Schmid, S., Du, G., Brand, H. E. A., Pang, W. K., Peterson, V. K., Guo, Z. & Sharma, N. (2014). *J. Vis. Exp.* **93**, e52284.
Brown, I. D. & Altermatt, D. (1985). *Acta Cryst.* B**41**, 244–247.
Cai, L., An, K., Feng, Z., Liang, C. & Harris, S. J. (2013). *J. Power Sources*, **236**, 163–168.
Cai, L., Liu, Z., An, K. & Liang, C. (2013). *J. Mater. Chem. A*, **1**, 6908–6914.
Cho, J., Kim, Y. J., Kim, T.-J. & Park, B. (2001). *Angew. Chem.* **113**, 3471–3473.
Colin, J.-F., Godbole, V. & Novák, P. (2010). *Electrochem. Commun.* **12**, 804–807.
Dillow, C. (2014). *Tesla's Bet on Winning the Global Lithium Race*, http://www.cnbc.com/id/101505280#.
Dolotko, O., Senyshyn, A., Mühlbauer, M. J., Nikolowski, K. & Ehrenberg, H. (2014). *J. Power Sources*, **255**, 197–203.
Dolotko, O., Senyshyn, A., Muhlbauer, M. J., Nikolowski, K., Scheiba, F. & Ehrenberg, H. (2012). *J. Electrochem. Soc.* **159**, A2082–A2088.
Du, G., Sharma, N., Peterson, V. K., Kimpton, J. A., Jia, D. & Guo, Z. (2011). *Adv. Funct. Mater.* **21**, 3990–3997.
Godbole, V. A., Heß, M., Villevieille, C., Kaiser, H., Colin, J.-F. & Novak, P. (2013). *RSC Adv.* **3**, 757–763.
Goodenough, J. B. & Kim, Y. (2011). *J. Power Sources*, **196**, 6688–6694.
Hu, C.-W., Sharma, N., Chiang, C.-Y., Su, H.-C., Peterson, V. K., Hsieh, H.-W., Lin, Y.-F., Chou, W.-C., Shew, B.-Y. & Lee, C.-H. (2013). *J. Power Sources*, **244**, 158–163.
Kim, J. H., Myung, S. T., Yoon, C. S., Kang, S. G. & Sun, Y. K. (2004). *Chem. Mater.* **16**, 906–914.
Kim, J.-H., Yoon, C. S., Myung, S.-T., Prakash, J. & Sun, Y.-K. (2004). *Electrochem. Solid State Lett.* **7**, A216–A220.
Laumann, A., Boysen, H., Bremholm, M., Fehr, K. T., Hoelzel, M. & Holzapfel, M. (2011). *Chem. Mater.* **23**, 2753–2759.
Le, M.-L.-P., Strobel, P., Colin, C. V., Pagnier, T. & Alloin, F. (2011). *J. Phys. Chem. Solids*, **72**, 124–135.
Liss, K.-D., Hunter, B., Hagen, M., Noakes, T. & Kennedy, S. (2006). *Physica B*, **385–386**, 1010–1012.
Liu, H., Fell, C. R., An, K., Cai, L. & Meng, Y. S. (2013). *J. Power Sources*, **240**, 772–778.
Ohzuku, T., Takeda, S. & Iwanaga, M. (1999). *J. Power Sources*, **81–82**, 90–94.
Ohzuku, T., Ueda, A. & Yamamoto, N. (1995). *J. Electrochem. Soc.* **142**, 1431–1435.
Panero, S., Reale, P., Ronci, F., Scrosati, B., Perfetti, P. & Rossi Albertini, V. (2001). *Phys. Chem. Chem. Phys.* **3**, 845–847.
Pang, W. K., Alam, M., Peterson, V. K. & Sharma, N. (2014). *J. Mater. Res.* doi:10.1557/jmr.2014.297.
Pang, W. K., Kalluri, S., Peterson, V. K., Dou, S. X. & Guo, Z. (2014). *Phys. Chem. Chem. Phys.* **16**, 25377–25385.
Pang, W. K., Peterson, V. K., Sharma, N., Shiu, J.-J. & Wu, S.-H. (2014*a*). *Chem. Mater.* **26**, 2318–2326.
Pang, W. K., Peterson, V. K., Sharma, N., Shiu, J.-J. & Wu, S.-H. (2014*b*). *Powder Diffr.* **29**, S59–S63.
Pang, W. K., Sharma, N., Peterson, V. K., Shiu, J.-J. & Wu, S.-H. (2014). *J. Power Sources*, **246**, 464–472.
Pasero, D., Reeves, N., Pralong, V. & West, A. R. (2008). *J. Electrochem. Soc.* **155**, A282–A291.
Ponrouch, A., Goñi, A. R. & Palacín, M. R. (2013). *Electrochem. Commun.* **27**, 85–88.
Roberts, M., Biendicho, J. J., Hull, S., Beran, P., Gustafsson, T., Svensson, G. & Edström, K. (2013). *J. Power Sources*, **226**, 249–255.
Rodriguez, M. A., Ingersoll, D., Vogel, S. C. & Williams, D. J. (2004). *Electrochem. Solid State Lett.* **7**, A8–A10.
Rodriguez, M. A., Van Benthem, M. H., Ingersoll, D., Vogel, S. C. & Reiche, H. M. (2010). *Powder Diffr.* **25**, 143–148.
Ronci, F., Reale, P., Scrosati, B., Panero, S., Rossi Albertini, V., Perfetti, P., di Michiel, M. & Merino, J. M. (2002). *J. Phys. Chem. B*, **106**, 3082–3086.
Rosciano, F., Holzapfel, M., Scheifele, W. & Novák, P. (2008). *J. Appl. Cryst.* **41**, 690–694.
Scharner, S., Weppner, W. & Schmid-Beurmann, P. (1999). *J. Electrochem. Soc.* **146**, 857–861.
Senyshyn, A., Dolotko, O., Muhlbauer, M. J., Nikolowski, K., Fuess, H. & Ehrenberg, H. (2013). *J. Electrochem. Soc.* **160**, A3198–A3205.
Senyshyn, A., Mühlbauer, M. J., Dolotko, O., Hofmann, M., Pirling, T. & Ehrenberg, H. (2014). *J. Power Sources*, **245**, 678–683.
Senyshyn, A., Mühlbauer, M. J., Nikolowski, K., Pirling, T. & Ehrenberg, H. (2012). *J. Power Sources*, **203**, 126–129.
Sharma, N., Du, G., Studer, A. J., Guo, Z. & Peterson, V. K. (2011). *Solid State Ionics*, **199–200**, 37–43.
Sharma, N., Guo, X., Du, G., Guo, Z., Wang, J., Wang, Z. & Peterson, V. K. (2012). *J. Am. Chem. Soc.* **134**, 7867–7873.

Sharma, N. & Peterson, V. K. (2012). *J. Solid State Chem.* **16**, 1849–1856.
Sharma, N. & Peterson, V. K. (2013*a*). *Electrochim. Acta*, **101**, 79–85.
Sharma, N. & Peterson, V. K. (2013*b*). *J. Power Sources*, **244**, 695–701.
Sharma, N., Peterson, V. K., Elcombe, M. M., Avdeev, M., Studer, A. J., Blagojevic, N., Yusoff, R. & Kamarulzaman, N. (2010). *J. Power Sources*, **195**, 8258–8266.
Sharma, N., Reddy, M. V., Du, G., Adams, S., Chowdari, B. V. R., Guo, Z. & Peterson, V. K. (2011). *J. Phys. Chem. C*, **115**, 21473–21480.
Sharma, N., Yu, D., Zhu, Y., Wu, Y. & Peterson, V. K. (2013). *Chem. Mater.* **25**, 754–760.
Shiu, J.-J., Pang, W. K. & Wu, S. (2013). *J. Power Sources*, **244**, 35–42.
Studer, A. J., Hagen, M. E. & Noakes, T. J. (2006). *Physica B*, **385–386**, 1013–1015.
Tarascon, J. M. & Armand, M. (2001). *Nature*, **414**, 359–367.
Tesla Motors (2014). *Model S*, http://www.teslamotors.com/models/features#/battery.
Vadlamani, B., An, K., Jagannathan, M. & Chandran, K. S. R. (2014). *J. Electrochem. Soc.* **161**, A1731–A1741.
Venugopal, G., Moore, J., Howard, J. & Pendalwar, S. (1999). *J. Power Sources*, **77**, 34–41.
Wang, X.-L., An, K., Cai, L., Feng, Z., Nagler, S. E., Daniel, C., Rhodes, K. J., Stoica, A. D., Skorpenske, H. D., Liang, C., Zhang, W., Kim, J., Qi, Y. & Harris, S. J. (2012). *Sci. Rep.* **2**, 747.
Yabuuchi, N., Kajiyama, M., Iwatate, J., Nishikawa, H., Hitomi, S., Okuyama, R., Usui, R., Yamada, Y. & Komaba, S. (2012). *Nat. Mater.* **11**, 512–517.
Zhang, S. S. (2007). *J. Power Sources*, **164**, 351–364.
Zinth, V., von Lüders, C., Hofmann, M., Hattendorff, J., Buchberger, I., Erhard, S., Rebelo-Kornmeier, J., Jossen, A. & Gilles, R. (2014). *J. Power Sources*, **271**, 152–159.